Doubly fed induction generator using back-to-back PWM converters and its application to variable-speed wind-energy generation

R.Pena
J.C.Clare
G.M.Asher

Indexing terms: Doubly fed induction motor, PWM converters, Vector control, Wind energy

Abstract: The paper describes the engineering and design of a doubly fed induction generator (DFIG), using back-to-back PWM voltage-source converters in the rotor circuit. A vector-control scheme for the supply-side PWM converter results in independent control of active and reactive power drawn from the supply, while ensuring sinusoidal supply currents. Vector control of the rotor-connected converter provides for wide speed-range operation; the vector scheme is embedded in control loops which enable optimal speed tracking for maximum energy capture from the wind. An experimental rig, which represents a 7.5kW variable speed wind-energy generation system is described, and experimental results are given that illustrate the excellent performance characteristics of the system. The paper considers a grid-connected system; a further paper will describe a stand-alone system.

List of symbols

V_s = RMS stator voltage
V_r = RMS rotor voltage
m_1, m_2 = stator and rotor converter modulation depths
E = DC link voltage
s = slip
n = stator – rotor turns ratio
L, R = inductance and resistance of supply side inductors
v_a, v_b, v_c = 3-phase supply voltages
v_d, v_q, v_α, v_β = 2-axis supply voltages
v_{a1}, v_{b1}, v_{b1} = 3-phase stator converter terminal voltages
v_{d1}, v_{q1} = 2-axis stator converter terminal voltages
i_a, i_b, i_c= 3-phase stator converter input currents
i_d, i_q = 2-axis stator converter input currents

IEE Proceedings online no. 19960288
Paper received 27th July 1995

The authors are with the Department of Electrical & Electronic Engineering, The University of Nottingham, University Park, Nottingham NG7 2RD, UK

ω_e, ω_r, ω_{slip} = supply, rotor, slip angular frequency
P, Q = active and reactive power
θ_e, θ_s = supply voltage, stator flux vector position
i_{os}, i_{or} = stator and rotor converter DC-link currents
C = DC-link capacitance
$F(s)$, $F(z)$ = plant-transfer functions
$G(z)$ = controller-transfer function
ζ = damping factor
λ = flux linkage
L_s, L_r, L_m, L_o = machine inductances per phase
R_s, R_r = machine resistances per phase
σ = leakage factor
i_{ms} = stator magnetising current
P = pole pairs
K_c, K_i, K_e, K_ω = controller gains
a_c, a_i, a_e, a_ω = controller parameters
P_m, P_{opt}, P_{max} = mechanical, optimum, maximum power
C_p, λ, β, r = turbine power coefficient, tip speed ratio, pitch angle, radius
v = wind velocity
B, J = friction, inertia
T_e, T_m = electromagnetic, mechanical torque
T_{aux} = auxiliary torque variable
K_{o1}, K_{o2} = Kalman-filter gains

Suffices, Superscripts
d, q = d–q axis
s, r = stator, rotor
$\hat{}$ = estimated value
$\sim$ = predicted value
$*$ = demanded (reference) value

1 Introduction

The doubly fed induction machine using an AC–AC converter in the rotor circuit (Scherbius drive) has long been a standard drive option for high-power applications involving a limited speed range. The power converter need only be rated to handle the rotor power. Vector-control techniques for the independent control of torque and rotor excitation current are well known [1], whilst Jones and Jones [2], for example, have shown that a vector-control strategy can be used for decoupled control of active and reactive power drawn from the supply. Wind-energy generation is regarded as a

natural application for the Scherbius DFIG system, since the speed range (from cut-in to rated wind velocity) may be considered restricted. Most Scherbius DFIG systems reported employ either a current-fed (naturally commutated) DC-Link converter [3–5] or cycloconverter [6–9] in the rotor circuit. Smith *et al.* [3] describe the rated speed settings, gearbox ratios, and machine and converter ratings for variable-speed wind generation using the DFIG. Cardici and Ermis [4], and Uctug *et al.* [5], have presented strategies aimed at maximising the total electrical power output from the DFIG. The use of a current-fed DC-link converter has a number of disadvantages: the DC-link choke is expensive, and an extra commutation circuit is required for operation at synchronous speed (which lies within the operational speed range), and this has resulted in poor performance at low slip speeds [4]. In addition, such a converter draws rectangular current waveforms from the supply. The problem at synchronous speed may be overcome by use of a cycloconverter, and vector-controlled Scherbius schemes with 6-pulse cycloconverters have been described by Leonhard [1] and Walczyna [6]. Yamamoto and Motoyoshi [7] have presented a detailed analysis of the current harmonics drawn from the supply, which is still a problem in this type of drive. Machmoum *et al.* [8] have presented an implementation with a simpler 3-pulse cycloconverter, whilst Holmes and Elsonbaty [9] describe a similar converter to excite a divided-winding doubly-fed machine, which improves the speed range to 50% slip at the expense of increased machine complexity. Both of these schemes have the disadvantage of requiring a transformer to form the neutral; in addition, naturally commutated DC-link and cycloconverter schemes may, in many cases, require a transformer for voltage matching.

The disadvantages of the naturally commutated DC-link and cycloconverter schemes can be overcome by the use of two PWM voltage-fed current-regulated inverters connected back-to-back in the rotor circuit. The characteristics of such a Scherbius scheme, in which both converters are vector controlled, are as follows:

- operation below, above and through synchronous speed with the speed range restricted only by the rotor-voltage ratings of the DFIG
- operation at synchronous speed, with DC currents injected into the rotor with the inverter working in chopping mode
- low distortion stator, rotor and supply currents
- independent control of the generator torque and rotor excitation
- Control of the displacement factor between the voltage and the current in the supply converter, and hence control over the system power factor.

Surprisingly, given the obvious advantages, Scherbius schemes using this arrangement have received little attention in the literature. Such a scheme was reported by Bogalecka [10] and Tang and Xu [11], using simulation studies, but the authors have not verified the performance of the system experimentally. In this paper, a full engineering study of an experimental back-to-back PWM vector Scherbius scheme is presented, with experimental results verifying the performance flexibility of the system. Since the research was initiated as part of a research program into new generator schemes for wind energy, the paper describes an implementation directed at wind generation, with the restriction that the system is connected to a grid. A stand-alone implementation is beyond the scope of the paper, and will be described in a future publication.

2 Experimental system

A schematic diagram of the overall system is shown in Fig. 1. The DFIG used was a 7.5kW, 415V, 50Hz 6-pole machine, whose parameters are given in the Appendix. Two voltage-fed PWM converters are inserted in the rotor circuit, with the supply-side PWM converter connected to the stator/supply via three single-phase chokes. The voltage-transfer characteristics

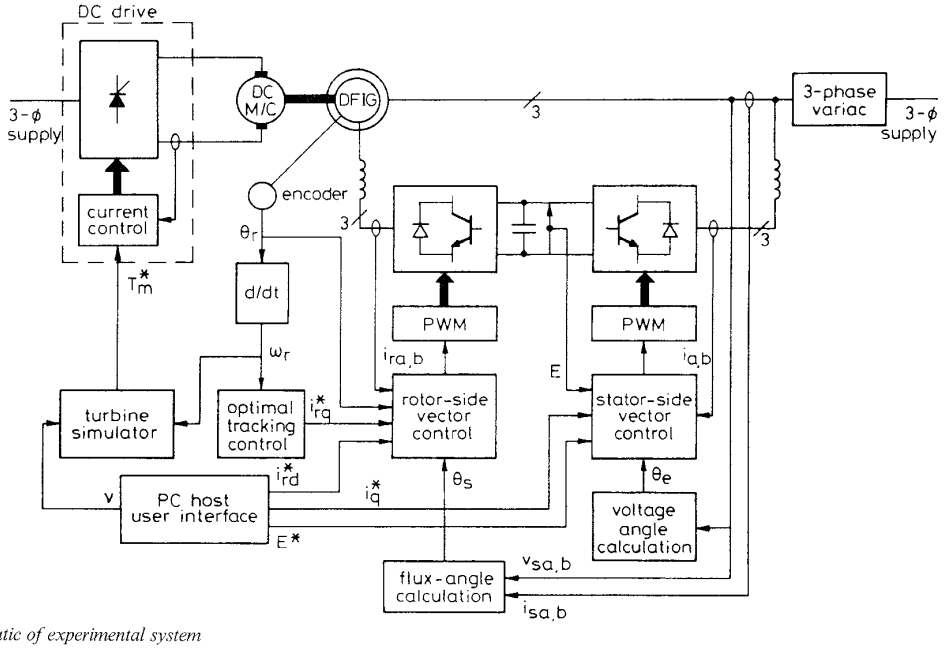

Fig. 1 *Schematic of experimental system*

of the system, including the 3-phase back-to-back PWM converters, are given approximately by

$$V_s = m_1 \frac{\sqrt{3}E}{2\sqrt{2}} \quad V_r = \pm s\frac{V_s}{n} = m_2 \frac{E}{2\sqrt{2}} \Rightarrow s = \pm \frac{nm_2}{\sqrt{3}m_1} \tag{1}$$

where n is the stator–rotor turns ratio of the DFIG (1.7 for the machine used), s is the slip and m_1, m_2 are the PWM modulation depths of the stator–side and rotor–side converters respectively. Eqn. 1 determines the speed range of the generator. The stator–side converter modulation depth is nominally 0.75 (as discussed below), and the maximum modulation depth for the rotor–side converter is approximately 0.76. This gives a theoretically possible speed range of 0 to 2000rpm for the 6-pole machine. In fact a lower speed range is used in practice since a full speed range from zero to twice-rated requires the PWM converters to be of equal rating to the machine, and this undermines the advantage of the Scherbius scheme. For wind generation, a restricted speed range is acceptable on account of a minimum wind velocity (the cut-in speed), below which very little energy is extractable. The generator speed corresponding to rated wind velocity can be set at any point by the choice of gearbox ratio. Of course, to get the maximum benefit from the Scherbius scheme, this point should be well above synchronous speed where power is extracted from both the rotor and stator of the machine. Eventually, however, as the slip is increased, the system efficiency starts to decrease since more power passes through the DC link converters and the rotor iron and frictional losses increase. For the machine and converters used in this study, the most efficient speed has been determined by experiment to be near 1500rpm and is therefore chosen to correspond with rated wind velocity. The turbine-gearbox arrangement is simulated in the experimental system by a thyristor converter fed DC machine which emulates a 7.5kW turbine with cut-in and rated wind velocities of $4ms^{-1}$ and $10ms^{-1}$, respectively, corresponding with generator speeds of 500 and 1500rpm.

The converters used are standard 7.5kW commercial bipolar transistor PWM inverters with a rated DC-link voltage of 580V and a maximum switching frequency of 1kHz. At this power level, the use of IGBT converters would have allowed a higher switching frequency and would have eased some of the control-loop design. However, the low switching frequency employed in the prototype confirms that the techniques used could be translated to much higher power levels using, for instance, GTO devices. In order to protect the inverter power devices, V_s (and hence V_r) was limited to approximately 250V line through a 3-phase variac on the supply, as shown in Fig. 1. The DC-link voltage was regulated to 550V with the supply side converter operating at a nominal modulation depth of 0.75, which allows sufficient latitude during transients to avoid problems with overmodulation. The use of 1200V devices in the converters would, of course, allow a DC-link voltage exceeding 700V to be obtained and thus obviate the need for a variac and allow the generator to operate at its full rating. Another practical problem was the presence of motor winding/slot harmonics in the induced rotor voltage, which was found to cause unacceptable rotor current oscillations at speeds over 1300rpm. This was solved by adding extra inductance (32mH/phase) in series with the rotor, as shown in Fig. 1. At lower speeds, acceptable rotor current waveforms are obtained, since the unwanted harmonics have a lower amplitude and are within the current control-loop bandwidth. The presence of these inductors means that the rotor-side converter modulation depth is slightly higher than that given by eqn. 1. The inductors in series with the supply-side converter are 12mH/phase, which limit the high-frequency ripple due to switching harmonics to 3A p-p (approximately 15% of the rated peak current). Since the high-frequency ripple is relatively small, the inductors can be fabricated using standard 50Hz lamination material without undue power loss.

The generator is driven by a torque-controlled 15kW DC motor drive, which simulates a wind turbine. A microprocessor receives wind-velocity data from a PC, and calculates the instantaneous turbine torque from a given turbine-blade characteristic (see the Appendix). This torque forms the torque demand to the DC drive after compensation for drive losses. The speed of the turbine-generator set is determined by an optimal speed tracking algorithm that effects maximum energy capture from the wind; this is discussed in Section 5.

Other system set points input from the PC include the DC-link voltage, the reactive current drawn by the supply-side PWM converter (which indirectly controls the system power factor), and the rotor excitation current that is nominally set to zero (see Section 4). The microprocessors used in the experimental rig are T800 floating point transputers, whose parallel processing capability allows the computational tasks to be partitioned into parallel units. One transputer carries out the vector control and PWM generation of the supply-side PWM converter, a second is responsible for the vector control of the DFIG and the optimal speed-tracking algorithms, a third implements the PWM for the rotor-side converter (because the second has too much work to do already) whilst a fourth acts both as a turbine torque calculator for the DC drive (simulating the turbine-blade characteristics) and also as a supervisory buffer interfacing with a PC. The latter provides the user interface, in which all system variables can be displayed during system operation, whilst set-points and control parameters can likewise be changed on-line. Details of system synchronisation, intertransputer communications, and A/D and PWM interfaces can be found in [12]. For a practical system, the use of a single high-performance DSP is possibly sufficient to carry out the control tasks, and would be more economic than the use of transputers; however, the latter have significant advantages during system development. The PWM switching frequency was set at 1 kHz on account of the converters used. The sampling period for all currents and voltages, and all control loops is 500 μs, unless specified otherwise.

3 Control of supply-side PWM converter

The objective of the supply-side converter is to keep the DC-link voltage constant regardless of the magnitude and direction of the rotor power. A vector-control approach is used, with a reference frame oriented along the stator (or supply) voltage vector position, enabling independent control of the active and reactive power flowing between the supply and the supply-side converter. The PWM converter is current regulated, with the direct axis current used to regulate the DC-link voltage and the quadrature axis current component

used to regulate the reactive power. A standard regular asymmetric sampling PWM scheme [13] is used. Fig. 2 shows the schematic of the supply-side converter. The voltage balance across the inductors is

$$\begin{bmatrix} \nu_a \\ \nu_b \\ \nu_c \end{bmatrix} = R \begin{bmatrix} i_a \\ i_b \\ i_c \end{bmatrix} + L\frac{\mathrm{d}}{\mathrm{d}t}\begin{bmatrix} i_a \\ i_b \\ i_c \end{bmatrix} + \begin{bmatrix} \nu_{a1} \\ \nu_{b1} \\ \nu_{c1} \end{bmatrix} \tag{2}$$

where L and R are the line inductance and resistance, respectively. Using the transformations of the Appendix, eqn. 2 is transformed into a dq reference frame rotating at ω_e:

$$\begin{aligned} \nu_d &= Ri_d + L\frac{\mathrm{d}i_d}{\mathrm{d}t} - \omega_e L i_q + \nu_{d1} \\ \nu_q &= Ri_q + L\frac{\mathrm{d}i_q}{\mathrm{d}t} + \omega_e L i_d + \nu_{q1} \end{aligned} \tag{3}$$

With the scaling factors used in the transformations of the Appendix, the active and reactive power flow is

$$\begin{aligned} P &= 3(\nu_d i_d + \nu_q i_q) \\ Q &= 3(\nu_d i_q + \nu_q i_d) \end{aligned} \tag{4}$$

The angular position of the supply voltage is calculated as

$$\theta_e = \int \omega_e \mathrm{d}t = \tan^{-1}\frac{\nu_\beta}{\nu_\alpha} \tag{5}$$

where ν_α and ν_β are the α, β (stationary 2-axis) stator-voltage components.

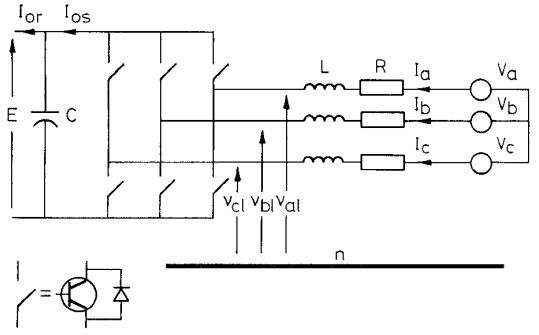

Fig. 2 *Supply-side converter arrangement*

Aligning the d-axis of the reference frame along the stator-voltage position given by eqn. 5, ν_q is zero, and, since the amplitude of the supply voltage is constant ν_d is constant. The active and reactive power will be proportional to i_d and i_q, respectively.

Neglecting harmonics due to switching and the losses in the inductor resistance and converter, we have

$$\begin{aligned} Ei_{os} &= 3\nu_d i_d \\ \nu_d &= \frac{m_1}{2\sqrt{2}}E \\ i_{os} &= \frac{3}{2\sqrt{2}}m_1 i_d \\ C\frac{\mathrm{d}E}{\mathrm{d}t} &= i_{os} - i_{or} \end{aligned} \tag{6}$$

From eqn. 6, it is seen that the DC-link voltage can be controlled via i_d. The control scheme thus utilises current control loops for i_d and i_q, with the i_d demand being derived from the DC-link voltage error through a standard PI controller. The i_q demand determines the displacement factor on the supply-side of the inductors. The strategy is shown in Fig. 3. From eqn. 3, the plant for the current control loops is given by:

$$F(s) = \frac{i_d(s)}{\nu'_d(s)} = \frac{i_q(s)}{\nu'_q(s)} = \frac{1}{Ls + R} \tag{7}$$

where

$$\begin{aligned} \nu^*_{d1} &= -\nu'_d + (\omega_e L i_q + \nu_d) \\ \nu^*_{q1} &= -\nu'_q - (\omega_e L i_d) \end{aligned} \tag{8}$$

In eqn. 8, ν^*_{d1} and ν^*_{q1} are the reference values for the supply-side converter, and the terms in brackets constitute voltage-compensation terms.

3.1 Control-loop designs

The design of the current controllers follows directly from eqn. 7, which can be written in the z-domain as

$$F(z) = \frac{(1-A)/R}{(z-A)} \quad A = e^{-(R/L)T_s} \tag{9}$$

where T_s is the sample time (0.5ms). The converter may be modelled by a pure delay of two sample periods yielding the control schematic of Fig. 4, for which

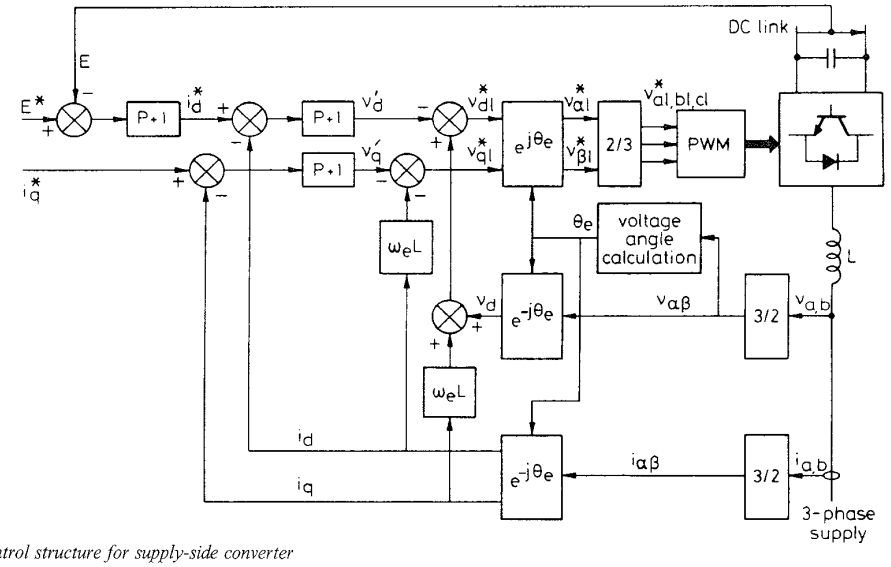

Fig. 3 *Vector-control structure for supply-side converter*

standard design techniques may be applied. For the inductors used, $R = 0.1\Omega$, $L = 12$mH, a design for a nominal closed-loop natural frequency of 125Hz and $\zeta = 0.8$ can be obtained using the PI controller:

$$G(z) = 4.72(z - 0.96)/(z - 1)$$

The design of the DC-link voltage controller may carried out in the continuous domain, and it is assumed that the inner i_d loop is ideal. From eqn. 6, the effective transfer function of the plant is

$$\frac{E(s)}{i_d(s)} = \frac{3m_1}{2\sqrt{2}Cs} \tag{10}$$

and the closed-loop block diagram is shown in Fig. 5, in which i_{or} is represented as a disturbance. Again, standard classical design is appropriate. Inserting values of $E^* = 550$V, $m_1 = 0.75$ (for $V_s = 250$V), $C = 2.4$mF and $T_s = 5$ms, a controller of $0.12\ (z - 0.9248)/(z - 1)$ can be shown to give a nominal closed-loop natural frequency of 25rads^{-1}, with $\zeta = 0.7$. This is 50 times slower than the loop sampling frequency, and justifies the continuous design.

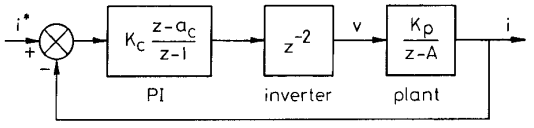

Fig.4 *Supply-side converter current-control loop*

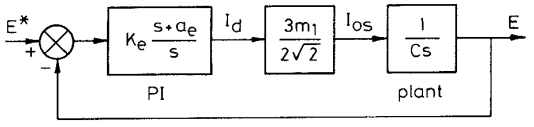

Fig.5 *DC-link voltage control loop*

3.2 Experimental results

Several tests have been carried out to study the performance of the supply-side converter in both transient and steady-state conditions, including bidirectional power flow with lagging, leading and a unity displacement factor. The DC-link voltage is regulated at 550V, and the converter is connected to a 250V supply.

Fig. 6 shows steady state results, with i_q^* set to zero, to give a unity displacement factor for the converter operating in the rectifying mode, which corresponds to subsynchronous operation of the generator. The steady state performance for the inverting operation mode corresponding to supersynchronous operation is shown in Fig. 7, with i_q^* also set to zero. In this case, the phase displacement between the phase voltage and the current is 180°.

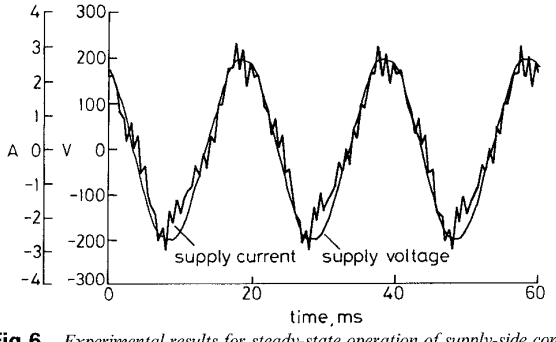

Fig.6 *Experimental results for steady-state operation of supply-side converter in rectifying mode*

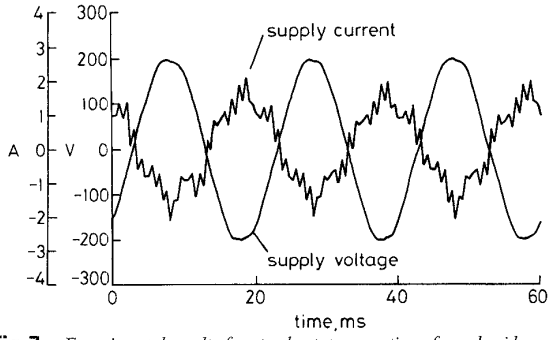

Fig.7 *Experimental results for steady-state operation of supply-side converter in inverting mode*

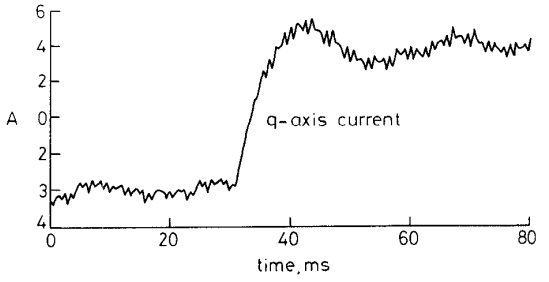

Fig.8 *Experimental response to step change in q-axis current demand*

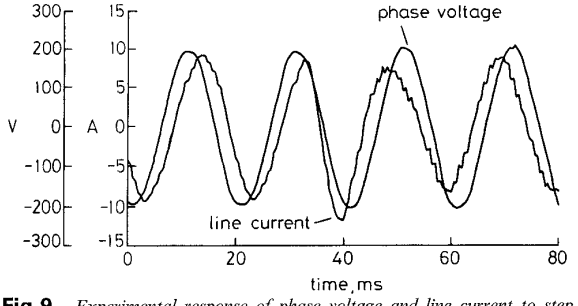

Fig.9 *Experimental response of phase voltage and line current to step change in q-axis current demand*

Fig. 8 shows the response of the converter to a step change in reactive current demand, with power flowing from the supply to the DC-link. Here i_d^* is set to 4.5A and i_q^* is stepped from −4A to +4A at $t = 30$ms. Fig. 9 shows the phase voltage and current, illustrating that the change in phase from 40° leading to 40° lagging takes place within one cycle. These waveforms demonstrate the capability of the converter to supply reactive power to, or receive reactive power from, the grid.

The same performance, although not shown, has been observed for step changes in reactive current demand, when the active power is flowing to the grid; the converter also being able to work at unity, lagging or leading power factor under that condition. The performance of the voltage-control loop is shown in Section 4.2.

4 Induction-machine control

The induction machine is controlled in a synchronously rotating dq axis frame, with the d-axis oriented along the stator-flux vector position. In this way, a decoupled control between the electrical torque and the rotor excitation current is obtained. The rotor-side PWM converter provides the actuation, and the control requires

the measurement of the stator and rotor currents, stator voltage and the rotor position. There is no need to know the rotor-induced EMF, as is the case for the implementation with naturally commutated converters.

Since the stator is connected to the grid, and the influence of the stator resistance is small, the stator magnetising current i_{ms} can be considered constant. Under stator-flux orientation, the relationship between the torque and the dq axis voltages, currents and fluxes (all scaled to be numerically equal to the AC per-phase values) may be written as [1]:

$$\begin{aligned}
\lambda_s &= \lambda_{ds} = L_o i_{ms} = L_s i_{ds} + L_o i_{dr} \\
\lambda_{dr} &= \frac{L_o^2}{L_s} i_{ms} + \sigma L_r i_{dr} \\
\lambda_{qr} &= \sigma L_r i_{qr} \\
i_{qs} &= -\frac{L_o}{L_s} i_{qr} \\
\nu_{dr} &= R_r i_{dr} + \sigma L_r \frac{\mathrm{d}i_{dr}}{\mathrm{d}t} - \omega_{slip} \sigma L_r i_{qr} \\
\nu_{qr} &= R_r i_{qr} + \sigma L_r \frac{\mathrm{d}i_{qr}}{\mathrm{d}t} + \omega_{slip}(L_m i_{ms} + \sigma L_r i_{dr}) \\
T_e &= -3\frac{P}{2} L_m i_{ms} i_{qr} \\
\omega_{slip} &= \omega_e - \omega_r \\
\sigma &= 1 - \frac{L_o^2}{L_s L_r} \\
L_m &= \frac{L_o^2}{L_s}
\end{aligned} \tag{11}$$

The stator flux angle is calculated from

$$\begin{aligned}
\lambda_{\alpha s} &= \int (v_{\alpha s} - R_s i_{\alpha s})\mathrm{d}t \\
\lambda_{\beta s} &= \int (v_{\beta s} - R_s i_{\beta s})\mathrm{d}t \\
\theta_s &= \tan^{-1} \frac{\lambda_{\beta s}}{\lambda_{\alpha s}}
\end{aligned} \tag{12}$$

where θ_s is the stator-flux vector position. The integral in eqn. 12 is solved using a digital passband filter, with cutoff frequencies of 0.5Hz and 1Hz to eliminate DC offsets. From eqn. 11, the torque is proportional to i_{qr} and can be regulated using ν_{qr}. The rotor excitation current i_{dr} is controlled using ν_{dr}. Assuming that all reactive power to the machine is supplied by the stator, i_{dr}^* may set to zero.

Fig. 10 shows a schematic block diagram for the machine control. The reference q-axis rotor current can be obtained either from a outer speed-control loop or from a reference torque imposed on the machine. These two options may be termed a speed-control mode or torque-control mode for the generator.

A similar analysis for the control of the dq currents carried out for the supply-side converter can likewise be done for the control of the dq rotor machine currents. From the rotor-voltage equation in eqn. 11 we have

$$\begin{aligned}
\nu'_{dr} &= R_r i_{dr} + \sigma L_r \frac{\mathrm{d}i_{dr}}{\mathrm{d}t} \\
\nu'_{qr} &= R_r i_{qr} + \sigma L_r \frac{\mathrm{d}i_{qr}}{\mathrm{d}t}
\end{aligned} \tag{13}$$

The i_{dr} and i_{qr} errors are processed by the PI controller to give ν_{dr} and ν_{qr}, respectively. To ensure good tracking of these currents, compensation terms are added to ν_{dr} and ν_{qr} to obtain the reference voltages ν_{dr}^* and ν_{qr}^* according to

$$\begin{aligned}
\nu_{dr}^* &= \nu'_{dr} - \omega_{slip} \sigma L_r I_{qr} \\
\nu_{qr}^* &= \nu'_{qr} + \omega_{slip}(L_m i_{ms} + \sigma L_r i_{dr})
\end{aligned} \tag{14}$$

which is analogous to eqn. 8.

4.1 Control-loop designs

The plant for the current-control design is similar to the case of the supply-side converter current controller (see Fig. 4) with the following variable substitutions:

$$\begin{aligned}
i_d, i_q &\rightarrow i_{dr}, i_{qr} \\
\nu'_d, \nu'_q &\rightarrow \nu'_{dr}, \nu'_{qr} \\
R &\rightarrow R_r \\
L &\rightarrow \sigma L_r \\
K_c &\rightarrow K_i \\
a_c &\rightarrow a_i
\end{aligned}$$

With T_s = 0.5ms and with the motor parameters of the Appendix, a nominal closed-loop natural frequency of

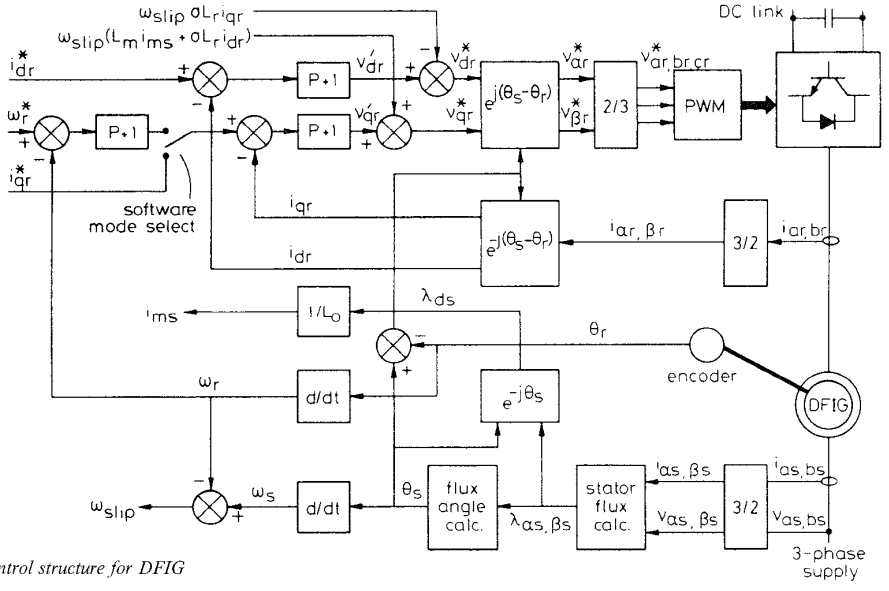

Fig. 10 *Vector-control structure for DFIG*

130Hz with $\zeta = 0.8$ is obtained, with the controller 20 $(z - 0.985)/(z - 1)$.

A speed controller is needed when the machine operates in the speed-control mode. The design of the speed controller is carried out in the continuous domain, in a similar way to that of the voltage controller for the supply-side converter, assuming also that the current controllers are much faster than the speed loop, and are thus considered ideal. The second order system of Fig. 5 is obtained (without the i_{or} disturbance) with the following variable substitutions:

$$E \rightarrow \omega_r$$
$$i_d \rightarrow i_{qr}$$
$$\frac{3m_1}{2\sqrt{2}} \rightarrow \frac{-3p}{2} L_m i_{ms}$$
$$i_{os} \rightarrow T_e$$
$$\frac{1}{Cs} \rightarrow \frac{1}{Js + B}$$
$$K_e \rightarrow K_\omega$$
$$a_e \rightarrow a_\omega$$

The rotor speed is obtained from a rotor-position measurement, which provides 720 pulses per revolution. With a sample time of 0.1s a resolution of 0.833rpm is obtained. The magnetising current can be obtained as $i_{ms} = V_s/\omega_e L_o$. With $T_s = 0.1$s, and with the appropriate parameters being given in the Appendix, a nominal closed-loop natural frequency of 0.05Hz with $\zeta = 0.9$ is obtained, with the controller 0.49 $(z - 0.988)/(z - 1)$. Although a faster speed controller can be designed for the speed-control mode, in practice it is found that noise considerations limit the closed-loop natural frequency. This derives from the fact that the speed demand is obtained from a mechanical torque observer, which effectively estimates the shaft acceleration from a limited-resolution speed encoder [14].

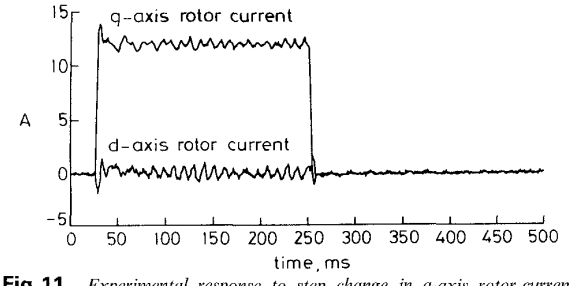

Fig. 11 *Experimental response to step change in q-axis rotor-current demand*

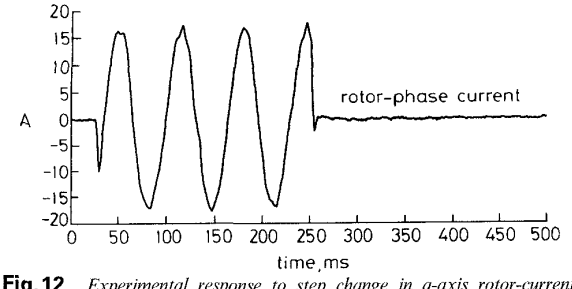

Fig. 12 *Experimental response to step change in q-axis rotor-current demand showing the rotor-phase current*

4.2 Experimental results

Results are given showing the step-current response for the DFIG for sub- and supersynchronous operation.

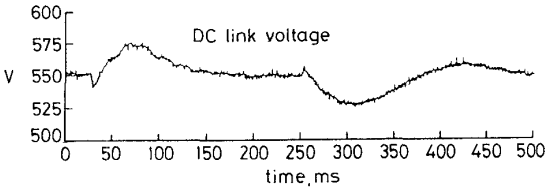

Fig. 13 *Experimental response to step change in q-axis rotor-current demand showing the DC link voltage E*

For these tests, the DFIG is driven by the DC machine under speed control. Figs. 11–13 show the response to a 12A (110% rated) step in i^*_{qr} applied at $t = 25$ms and removed at $t = 250$ms for supersynchronous operation ($\omega_r = 1300$rpm), with the excitation rotor current i_{dr} maintained at zero. Fig. 12 shows the rotor-phase current and Fig. 13 the DC-link voltage E. These transients represent the worst case for the stator converter voltage-control loop, where the DC-link power is stepped from zero to rated and vice versa. As shown, the maximum error in the DC-link voltage is 25V (4.5% of nominal) and recovery takes place within 200ms, which is consistent with the control-loop design.

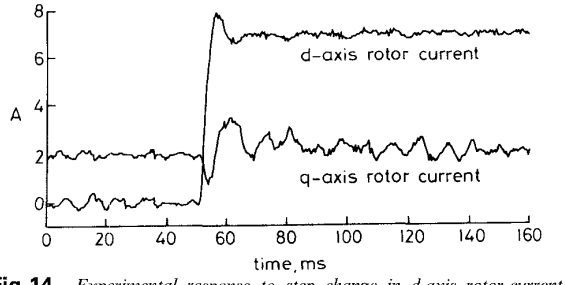

Fig. 14 *Experimental response to step change in d-axis rotor-current demand*

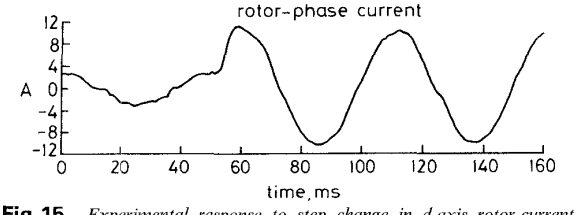

Fig. 15 *Experimental response to step change in d-axis rotor-current demand showing the rotor-phase current*

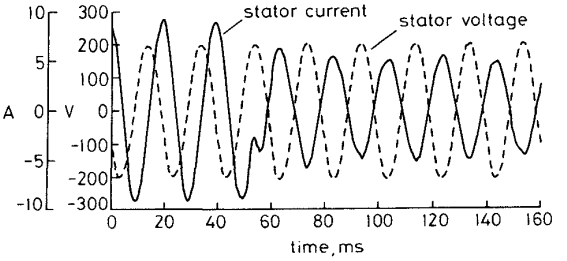

Fig. 16 *Experimental response to step change in d-axis rotor-current demand showing the stator voltage and current*

Although the magnetising current in a DFIG is normally determined by the stator voltage, the freedom exists to control the magnetising current from i_{dr}. Figs. 14–16 show the response to a step change in i^*_{dr} of 7 A (which corresponds to rated magnetising current referred to the rotor) at $t = 50$ ms for subsynchronous operation ($\omega_r = 600$ rpm) with i_{qr} maintained at 2 A.

Fig. 15 shows the rotor-phase current and Fig. 16 shows the stator voltage and current on the same time axis. As is evident from the phase displacement, the magnetising current is initially supplied from the stator until t = 50 ms, where the phase shift changes to 180°, showing that the machine is generating with all the magnetising current supplied from the rotor. In practice, it is generally desirable to supply the magnetising current entirely from the stator (by setting i^*_{dr} = 0) to minimise the losses in the rotor converter cascade.

One of the advantages of this PWM Scherbius scheme is the smooth operation through synchronous speed; this is shown in Fig. 17.

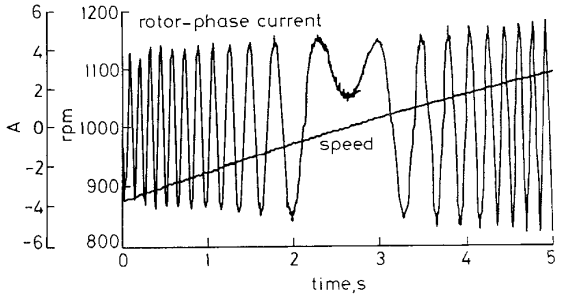

Fig. 17 *Experimental results for operation through synchronous speed*

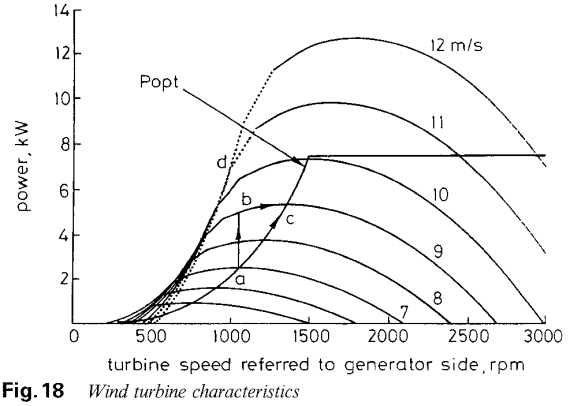

Fig. 18 *Wind turbine characteristics*

5 Optimum operating point tracking of a variable-speed wind turbine

Optimal tracking to provide maximum energy capture from the wind derives from the power-speed characteristics of a given turbine. This is commonly expressed as [15]:

$$P_m = \frac{1}{2} C_p(\lambda, \beta) \pi \rho r^2 v^3 \tag{15}$$

The turbine blade is characterised by particular C_p–λ, β curves, and from these the T_m–ω_r characteristics may be derived for various values of wind velocity v. Fig. 18 shows the characteristic, with a fixed β, for the 7.5kW wind turbine emulated in the experimental rig. The curve P_{opt} defines the maximum energy capture, and the objective of a tracking control is to keep the turbine on this curve as the wind velocity varies. The curve is defined by [15]:

$$P_{opt} = K_{opt}\omega_r^3 \quad \text{or} \quad T_{P_{opt}} = K_{opt}\omega_r^2 \tag{16}$$

where ω_r is the shaft speed referred to the generator side of the gearbox. For wind velocities higher than rated, the turbine energy capture must be limited by applying pitch control or driving the machine to the stall point [16–18]. For wind velocities below rated, the machine follows eqn. 16. There are two methods of achieving this which are termed 'current-mode control' or 'speed-mode control'.

5.1 Current-mode control

This mode may be considered to be standard tracking mode [17]. Given a shaft-speed measurement, an electrical torque can be imposed on the DFIG according to eqn. 16 after compensating for the transmission friction losses:

$$T_e^* = K_{opt}\omega_r^2 - B\omega_r \quad i_{qr}^* = \frac{-2T_e^*}{3pL_m i_{ms}} \tag{17}$$

and i^*_{qr} is impressed on the DFIG. Considering Fig. 18, if the DFIG is operating at 'a' and the wind increases from 7ms^{-1} to 8 ms^{-1} (point 'b'), the extra power and hence torque causes the DFIG to accelerate, the accelerating torque being the difference between the turbine mechanical torque and the torque given by the optimum curve. Eventually the machine will reach the point 'c' where the accelerating torque is zero. A similar situation occurs when the wind velocity decreases.

5.2 Speed-mode control

This is a rather novel method [14, 19] and has not hitherto received much attention on account of its requirement for a mechanical torque observer. The authors' research team have shown [14] that, whilst there are engineering problems associated with the observer design, the method is feasible in practice, and that significantly improved tracking may be obtained over the current-control method above. Given a T_m signal, then the DFIG can be driven to the optimum power curve by

$$\omega_r^* = \sqrt{\frac{T_m}{K_{opt}}} \tag{18}$$

where ω_r^* is the demand speed for the speed controller considered in Section 4.1. In this study the mechanical torque is observed using the mechanical model of the system given by

$$\frac{\mathrm{d}}{\mathrm{d}t}\begin{bmatrix}\tilde{\omega}_r \\ \tilde{T}_{aux}\end{bmatrix} = \begin{bmatrix}0 & \frac{1}{J} \\ 0 & 0\end{bmatrix}\begin{bmatrix}\tilde{\omega}_r \\ \tilde{T}_{aux}\end{bmatrix} - \begin{bmatrix}\frac{3pL_m i_{ms}}{2J} \\ 0\end{bmatrix} i_{qr}$$
$$[\tilde{\omega}_r] = [1 \quad 0]\begin{bmatrix}\tilde{\omega}_r \\ \tilde{T}_{aux}\end{bmatrix} \tag{19}$$

where $\tilde{\omega}_r$ is the predicted speed and $\tilde{T}_{aux}$ is a predicted auxiliary torque variable. The estimated speed $\hat{\omega}_r$ and mechanical torque $\hat{T}_m$ follow from

$$\begin{aligned}\hat{\omega}_r &= \tilde{\omega}_r + K_{o1}(\omega_r - \tilde{\omega}_r) \\ \hat{T}_{aux} &= \tilde{T}_{aux} + K_{o2}(\omega_r - \tilde{\omega}_r) \\ \hat{T}_m &= \hat{T}_{aux} + B\omega_r\end{aligned} \tag{20}$$

where k_{o1} and k_{o2} are constants defining the observer dynamics. These gains may be derived either by Kalman Filter [20] or classical observer design. For the parameters of Appendix 1, gain values of k_{o1} = 0.98 and k_{o2} = 5.9 give an observer dynamic natural frequency of about 4rads^{-1}.

5.3 Stall regulation

One of the advantages of a torque observer is that it allows the straightforward implementation of stall regulation as the method of overspeed protection. The

system calculates the instantaneous power $\hat{P}_m = \hat{T}_m\omega_r$, and hence determines the speed demand according to

$$\begin{aligned} &\text{if} \quad \hat{P}_m < P_{max} \quad \text{then} \quad \omega_r^* = \sqrt{\frac{\hat{T}_m}{K_{opt}}} \\ &\text{if} \quad \hat{P}_m \geq P_{max} \quad \text{then} \quad \omega_r^* = \frac{P_{max}}{\hat{T}_m} \end{aligned} \tag{21}$$

wherein if $\hat{P}_m \geq P_{max}$, energy capture is reduced through the DFIG being driven to the stall point (a sample stall point for a particular wind velocity is marked 'd' in Fig. 18). Stall regulation has the advantage over the alternative (and more usual) overspeed protection scheme of blade pitch control, in that simple fixed pitch blades may be used. However, stall regulation requires not only an effective torque estimator but also a sufficient generator overtorque capability to overcome the instantaneous turbine torque, and hence decelerate the system to the stall point. This in turn effects the choice of machine rating [21].

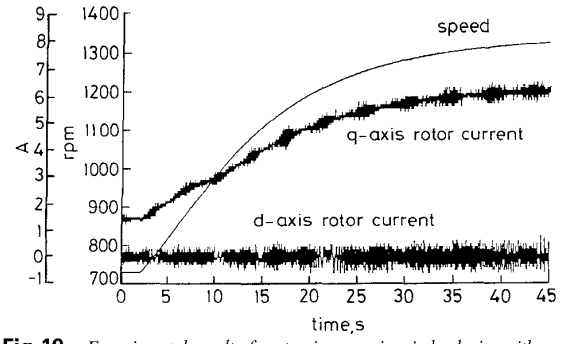

Fig. 19 *Experimental results for step increase in wind velocity with current-mode control*

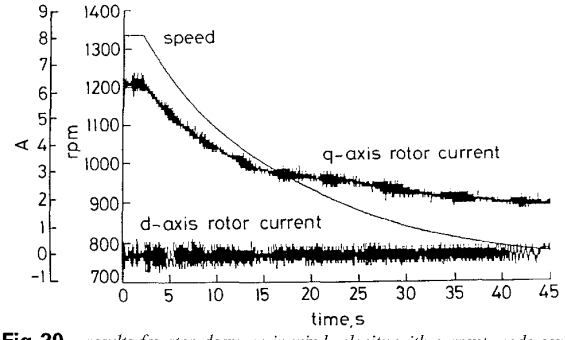

Fig. 20 *results for step decrease in wind velocity with current-mode control*

5.4 Experimental results

The transient performance of the system working in either control mode is evaluated for step wind velocity transients between 5ms^{-1} and 9ms^{-1}, corresponding to optimal shaft speeds of 750rpm and 1350rpm, respectively. The rotor excitation current $i_{dr}^* = 0$. Figs. 19 and 20 show the performance of the current-mode control, whilst Figs. 21 and 22 show the corresponding performance of the speed-mode control. The dynamic speed performance of the speed-mode control is clearly superior with the DFIG torque (i.e. i_{qr}) behaviour, being similar to that of a conventional speed-controlled servo drive; on acceleration, the torque is reduced to a minimum of zero, since the DFIG has not been allowed to motor (a superior response could of course be obtained if a negative limit is set for i_{qr}^*) whilst i_{qr} hits a maximum limit under deceleration. Under current-mode control, the torque capability of the machine is not exploited, and both the torque and speed hunt smoothly to the optimum curve.

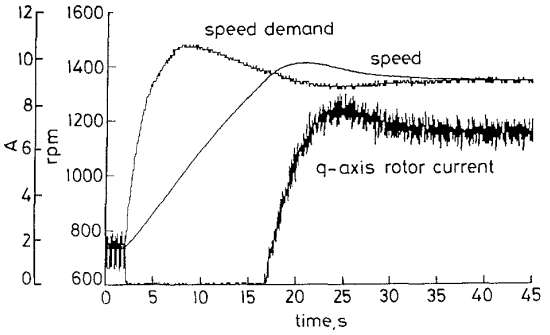

Fig. 21 *Experimental results for step increase in wind velocity with speed-mode control*

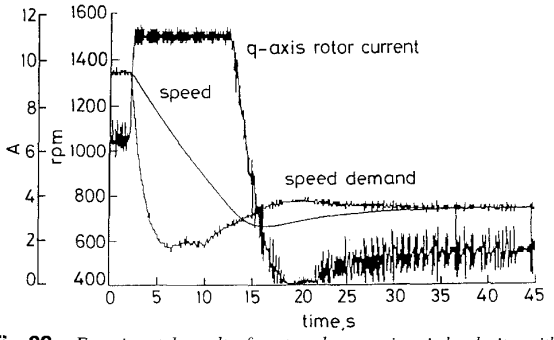

Fig. 22 *Experimental results for step decrease in wind velocity with speed-mode control*

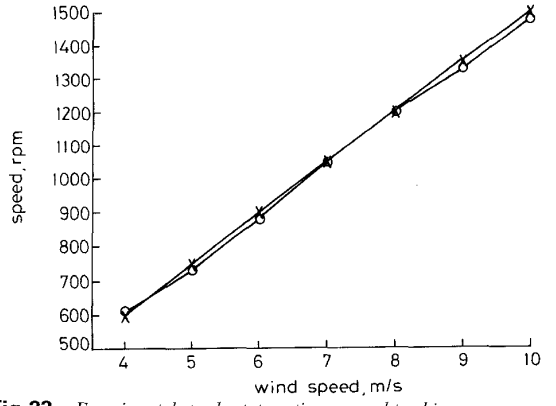

Fig. 23 *Experimental steady-state optimum speed tracking*
* optimum speed; O machine speed

Steady-state system characteristics have been studied, with the machine working on the optimal power curve under either control mode. Fig. 23 shows the optimal speed tracking for various wind velocities; the tracking accuracy depends on the accuracy in quantifying the power losses in the drive train. An accuracy of 4% is achieved using a look-up table for the torque compensation due to drive friction and machine iron losses. Fig. 24 shows the power output from the rotor, stator and supply-side (denoted 'front-end') converter. Above synchronous speed, power is generated both from the stator and the rotor. No power is generated when the wind velocity is below 5ms^{-1} (even when the machine is driven to the optimum power curve) because the

mechanical and electrical losses are higher than the power available from the wind. Fig. 25 shows the rotor current as a function of shaft speed. The rotor current follows a quadratic law as predicted for optimal tracking.

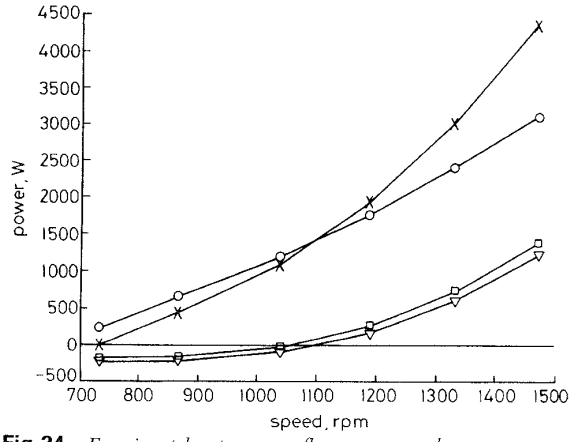

Fig. 24 *Experimental system power flows versus speed*
○ Pstator; □ Protor; ▽ Pfront - end; ✳ P - output

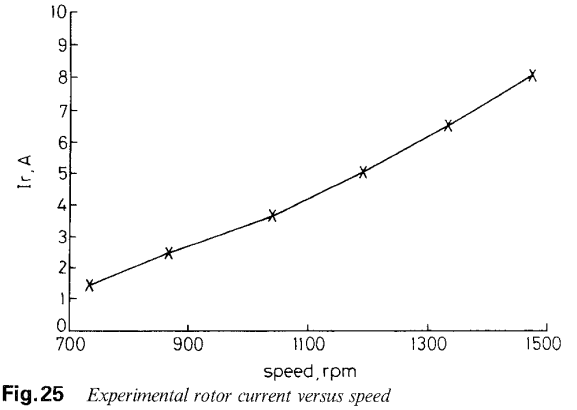

Fig. 25 *Experimental rotor current versus speed*

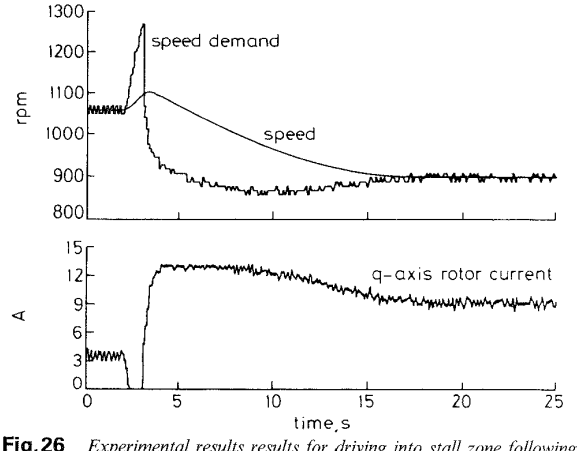

Fig. 26 *Experimental results results for driving into stall zone following a step increase in wind velocity*

Experimental results showing the performance of the system when driving into and out of the stall zone are presented. The maximum power has been set to a nominal P_{max} = 4kW, in order that the DFIG can produce sufficient decelerating torque. Fig. 26 shows the response to a step increase in wind velocity from 7ms^{-1} (for which $\hat{P}_m < P_{max}$) to 9ms^{-1} (for which $\hat{P}_m > P_{max}$). A wind velocity of 7ms^{-1} corresponds to an optimal shaft speed of 1050rpm. The torque current momentarily decreases in order to accelerate the machine to the new optimum speed according to eqn. 18, but when P_{max} is reached, the current increases to decelerate the DFIG into the stall zone. Following this, the current settles at a value which regulates the power to the nominal maximum. Fig. 27 shows the reverse situation for the DFIG being driven out of the stall zone under a wind velocity transient of 9ms^{-1} to 7ms^{-1}.

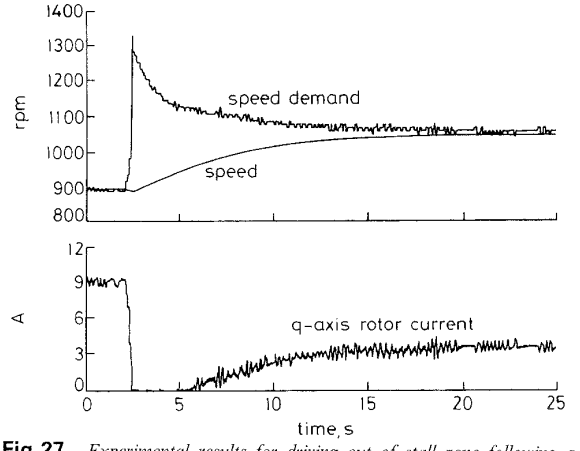

Fig. 27 *Experimental results for driving out of stall zone following a step decrease in wind velocity*

6 Conclusions

The engineering and design aspects of a DFIG working with a Scherbius scheme, consisting of two back-to-back PWM converters, has been presented. An experimental transputer controlled system has been described, and the fundamental operational advantages have been verified. These include the smooth operation through synchronous speed, low distortion currents fed to the supply and the ability to control the system power factor. Vector-control techniques have been applied to both converters. The vector control for the machine has been embedded in an optimal tracking controller for maximum energy capture in a wind-energy application. Two such tracking schemes have been described, and experimentally implemented, and the superiority of speed-mode control for dynamic speed performance has been shown. This scheme employs a torque observer, which also allows for simple implementation of stall regulation to protect against generator overload.

The present paper has described the back-to-back PWM DFIG scheme with the system grid connected. The scheme can also be used for supplying an isolated AC load, augmented with a controlled dump load. This will be the subject of a future paper.

7 Acknowledgments

The authors would like to thank Mr R. Moulding of Brush Industrial Controls Division for his useful contribution at the start of this work and for providing some of the equipment. Mr R. Pena would like to thank the University of Magallanes, Chile and the Chilean Government for financial support during the course of this work.

8 References

1 LEONHARD, W.: 'Control of electrical drives' (Springer–Verlag, 1985)
2 JONES, S.R., and JONES, R.: 'Control strategy for sinusoidal supply side convertors', IEE Colloquium on *Developments in real time control for induction motor drives*, Digest 1993/024, February 1993
3 SMITH, G.A., NIGIM, K., and SMITH, A.: 'Wind-energy recovery by a static Scherbius induction generator', *IEE Proc. C*, 1981, **128**, (6), pp. 317–324
4 CARDICI, I., and ERMIS, M.: 'Double-output induction generator operating at subsynchronous and supersynchronous speed: steady state performance optimisation and wind-energy recovery', *IEE proc. B*, 1992, **139**, (5), pp. 429–442
5 ÜÇTUG, M.Y., ESKANDARZADEH, I., and INCE, H.: 'Modelling and output power optimisation of a wind turbine driven double output induction generator', *IEE Proc. B*, 1994, **141**, (2)
6 WALCZYNA, A.M.: 'Torque and reactive power control of a double-fed induction machine', *BICEM Proc.*, 1987, pp. 495–498
7 MITSUTOSHI, Y., and MOTOYOSHI, O.: 'Active and reactive power control for doubly-fed wound rotor induction generator', *IEE Trans. Power Electron.*, 1991, **6**, (4), pp. 624–629
8 MACHMOUM, M., LE DOEUFF, R., SARGOS, F.M., and CHERKAOUI, M.: 'Steady state analysis of a doubly fed asynchronous machine supplied by a current controlled cycloconverter in the rotor', *IEE Proc. B*, 1992, **139**, (2), pp. 114–122
9 HOLMES, P.G., and ELSONBATY, N.A.: 'Cycloconverter excited divided winding doubly fed machine as a wind power converter', *IEE Proc. B*, 1984, **131**, (2), pp. 61-69
10 BOGALECKA, E.: 'Power control of a double fed induction generator without speed or position sensor', *EPE*, 1993, **8**, (377), Chap. 50, Pt 8, pp. 224–288
11 TANG, Y., and XU, L.: 'Stator field oriented control of doubly excited induction machine in wind power generating system', 35th Mid-West Symp. on *Circuits and systems*, Washington, DC, 1992, pp. 1446–1449
12 ASHER, G.M., and SUMNER, M.: 'Parallelism and the transputer for the real-time high performance control of AC induction motors', *IEE Proc. D*, 1990, **137**, (4), pp. 179–188
13 BOWES, S.R., and MOUNT, M.J.: 'Microprocessor control of PWM inverters', *IEE Proc. B*, 1981, **128**, (6), pp. 293–305
14 CARDENAS, R.: 'Control of wind turbines using switched reluctance generators'. PhD thesis, 1996, University of Nottingham, UK
15 WILMSHURST, S.M.B.: 'Control strategy for wind turbines', *Wind Eng.*, 1988, **12**, (4), pp. 236–250
16 LEITHEAD, W.E., DE LA SALLE, S.A., and REARDON, D.: 'Classical control of active pitch regulation of constant speed horizontal axis wind turbine', *Int. J. Control*, 1992, **55**, pp. 845–876
17 GOODFELLOW, D., and SMITH, G.A.: 'Control strategy for variable speed wind energy recovery', Proceeding of 8th BWEA Conf., Cambridge, 1986, pp. 219–228
18 THIRINGER, T., and JAN LINDERS, J.: 'Control by variable speed of a fixed-pitch wind turbine operating in a wide speed range', *IEE Trans. Energy Convers.*, 1993, **8**, (3), pp. 520–526
19 BUEHRING, K., and FRERIS, L.L.: 'Control policies for wind-energy conversion systems', *IEE Proc. C*, 1981, **128**, (5), pp. 253–261
20 BROWN, R.G., and HUANG, P.: 'Introduction to random signals and applied Kalman filtering' (John Wiley and Sons, 1992), 2nd edn.
21 PENA, R.: 'Power rating of double fed induction generator using stall regulation', Internal report, Dept. Elec. Eng., University of Nottingham, 1995

9 Appendices

9.1 (a) Experimental system ratings

Wind turbine (emulated by DC machine drive):

Power = 7.5kW
Radius = 3.24m
Rated rotational speed = 296rpm
Rated wind speed = $10 ms^{-1}$
Cut-in speed = $4 ms^{-1}$
Maximum speed = $12 ms^{-1}$
Inertia = $7.5 Kgm^2$
Gear box = 5.065
Friction coefficient = $0.06 Nmsrad^{-1}$

Wound rotor induction machine:

Power = 7.5kW
Stator voltage = 415V
Rotor voltage = 440V
Rated stator current = 19A
Rated rotor current = 11A
$R_s = 1.06\Omega$
$R_r = 0.80\Omega$
$L_s = 0.2065H$
$L_o = 0.0664H$ (referred to the rotor)
$L_r = 0.0810H$ (referred to the rotor)
$L_{ext} = 0.0320H$ (referred to the rotor)
Pole pairs = 3
Rated speed = 970rpm
Stator-rotor turns ratio n = 1.7
Stator connection = delta
Rotor connection = star

9.2 Reference frame transformations

Stationary abc reference frame to stationary αβ reference frame:

Voltages:

$$\nu_\alpha = \sqrt{3}\nu_{ab} + \frac{\sqrt{3}}{2}\nu_{bc}$$

$$\nu_\beta = \frac{3}{2}\nu_{bc}$$

Currents:

$$i_\alpha = \frac{3}{2}i_a$$

$$i_\beta = \frac{\sqrt{3}}{2}(i_b - i_c)$$

Stationary αβ reference frame to rotating *dq* reference frame:

Voltages (and currents):

$$\nu_d = \nu_\alpha \cos\theta - \nu_\beta \sin\theta$$

$$\nu_q = \nu_\beta \cos\theta + \nu_\alpha \sin\theta$$

where θ is the angular position of the *dq* reference frame.

Variable scaling: The *dq* variables are scaled to have the same amplitude as the phase quantities as follows:

$$\nu_d = \frac{\nu_d}{k_\nu} \quad \nu_q = \frac{\nu_q}{k_\nu} \quad i_d = \frac{i_d}{k_i} \quad i_q = \frac{i_q}{k_i}$$

where:

$k_v = (3/2)\sqrt{2}$ for delta connection
$k_v = (3/2)\sqrt{6}$ for star connection
$k_i = (3/2)\sqrt{6}$ for delta connection
$k_i = (3/2)\sqrt{2}$ for star connection.